Enhanced Graphical Representation of Electrochemical Impedance Data

Mark E. Orazem, Nadine Pébère, Bernard Tribollet

Enhanced Graphical Representation of Electrochemical Impedance Data

Mark E. Orazem,[a,*,z] Nadine Pébère,[b] and Bernard Tribollet[c,*]

[a]*Department of Chemical Engineering, University of Florida, Gainesville, Florida 32611, USA*
[b]*CIRIMAT, ENSIACET, UMR CNRS 5085, Toulouse Cedex 31077, France*
[c]*Laboratoire Interfaces et Systèmes Electrochimiques, UPR 15 du CNRS, Université Pierre et Marie Curie, 75252 Paris, France*

Bode plots, corrected for Ohmic resistance, logarithmic plots of the imaginary component of the impedance, and effective capacitance plots are shown to be useful complements to the more traditionally used complex-plane and Bode representations for electrochemical impedance data. The graphical methods are illustrated by synthetic data and by experimental data associated with corrosion in saline environments. Bode plots are shown, in particular, to be confounded by the influence of electrolyte resistance. The plots proposed here provide useful guides to model development for both reactive and blocking systems. The logarithmic plots of the imaginary component of the impedance and effective capacitance plots are useful for all impedance data, and the correction for Ohmic resistance in Bode plots is useful when the solution resistance is not negligible.
DOI: 10.1149/1.2168377

[12]Graphical methods provide the first step toward interpretation and evaluation of impedance data. A number of authors have described graphical methods based on a deterministic model for a given process. Mott-Shottky plots of $1/C_{sc}^2$ as a function of potential are used to obtain flatband potentials and doping levels characteristic of semiconducting systems.[1] A graphical method was reported by Tribollet et al. that can be used to extract Schmidt numbers from experimental data in which the convective diffusion impedance dominates.[2] The technique accounts for the finite value of the Schmidt number. Graphical methods in terms of a dimensionless frequency scaled by rotation speed are commonly used for the interpretation of electrohydrodynamic impedance measurements.[3] Jansen and Orazem describe a graphical superposition of impedance data collected at different temperatures that reveals the influence of a single dominant activation-energy controlled process in solid-state systems.[4]

When a specific model is not postulated, typically two types of graphical representations are used: complex-impedance-plane plots, often called Nyquist plots, and Bode plots.[5-7] The Bode representation consists of the logarithm of impedance magnitude and the phase angle, both plotted as a function of frequency on a logarithmic scale. These types of representation have become the standard in impedance analysis for any complex quantity, e.g., admittance, complex capacitance, and electrohydrodynamic impedance, as well as electrochemical impedance.

The object of this work is to demonstrate the limitations of the usual methods for representing impedance data and to suggest some useful alternatives. The proposed graphical methods are illustrated both by synthetic data and by experimental data associated with corrosion of a magnesium alloy AZ91 in saline environments.

Synthetic Data

The methods for graphical representation and interpretation of electrochemical impedance are presented here for data characteristic of active and blocking electrodes. The classification of active systems is represented by a Randles circuit, as presented in Fig. 1a. The classification of blocking systems is represented by the circuit presented in Fig. 1b.

Application to a Randles circuit.— A Randles circuit is used here to demonstrate the graphical representation for reactive (non-blocking) systems. The impedance of the Randles circuit presented in Fig. 1a is given by

$$Z(f) = R_e + \frac{[R_t + z_d(f)]}{1 + (j2\pi f)^{\alpha} Q[R_t + z_d(f)]} \qquad [1]$$

where the convective diffusion impedance $z_d(f)$ was given by the expression for a finite stagnant diffusion layer, i.e.

$$z_d(f) = z_d(0)\frac{\tanh(\sqrt{j2\pi f\tau_d})}{\sqrt{j2\pi f\tau_d}} \qquad [2]$$

and the parameters α and Q are associated with a constant-phase element (CPE).[7-9] When $\alpha = 1$, Q_{dl} has units of a capacitance, i.e., $\mu F\ cm^{-2}$, and represents the capacity of the double layer. When $\alpha \neq 1$, the system shows behavior that has been attributed to surface heterogeneity[10,11] or to continuously distributed time constants for charge-transfer reactions.[12-16] The phase angle associated with a CPE is independent of frequency.

The parameter values used for the simulations presented here are given in Table I. The parameters were chosen such that the high-frequency CPE element would have a characteristic frequency f_{RC} of 100 Hz, corresponding to a time constant of 1.59 ms.

The Randles circuit provides an example of a class of systems for which, at the zero-frequency or dc limit, the resistance to passage of current is finite, and current can pass. Many electrochemical and electronic systems exhibit such non-blocking or reactive behavior. Even though the impedance response of the system presented in this section is relatively simple as compared to that of typical electrochemical and electronic systems, the non-blocking systems comprise a broad cross section of electrochemical and electronic systems. The concepts described in the present work can therefore be easily adapted to experimental data.

Traditional representation of data.— Impedance data are often represented in complex-impedance-plane or Nyquist formats accompanied with Bode representations in which the modulus and phase angle are presented as a function of frequency.[5-7] Such traditional representations of impedance data are given in Fig. 2 for the circuit presented as Fig. 1a.

The complex-impedance-plane or Nyquist format is shown in Fig. 2a for the Randles circuit. The data are presented as a locus of points, where each data point corresponds to a different measurement frequency. The asymptotic limits of the real part of the impedance for the reactive circuit shown in Fig. 2a are R_e at high frequencies and $R_e + z_d(0) + R_t$ at low frequency. Impedance-plane plots are very popular because the shape of the locus of points yields insight into possible mechanisms or governing phenomena. If the locus of points traces a perfect semicircle, for example, the impedance response corresponds to a single activation-energy-controlled process. A depressed semicircle indicates that a more detailed model is required, and the multiple loops shown in Fig. 2a provide a clear

* Electrochemical Society Active Member.
z E-mail: meo@che.ufl.edu

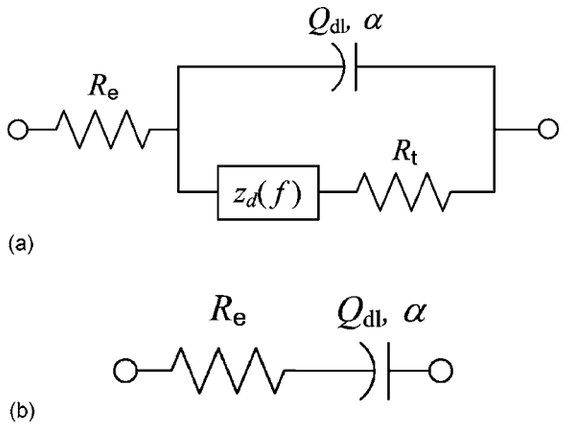

Figure 1. Equivalent circuits used to demonstrate the graphical representation of reactive impedance data: (a) Randles circuit; (b) blocking circuit.

indication that more than one time constant is required to describe the process. The significant disadvantages are that the frequency dependence is obscured, low impedance values are obscured, and the apparent agreement between model and experimental data in the complex-impedance-plane format may obscure large differences in frequency and at low impedance values.

The dependence on frequency is seen more clearly in the Bode representation shown in Fig. 2b and c for the magnitude and phase angle of the Randles circuit. Frequency is generally presented on a logarithmic scale to reveal the important behavior seen at lower frequencies. For a process described by a single *RC* element, the characteristic frequency is readily identified by inflections in the magnitude and phase-angle plots. The magnitude of the impedance of the single *RC* reactive system tends toward R_e as frequency tends toward ∞ and toward $R_e + R_t$ as frequency tends toward zero. The phase angle has a value of $-45°$ at the characteristic frequency $f_{RC} = 1/(2\pi RC)$. The slope of the transition between low-frequency and high-frequency asymptotes can provide useful information concerning the nature of the impedance response if the characteristic time constants are well separated.

The phase angle, expressed as

$$\phi = \tan^{-1}\left(\frac{Z_j}{Z_r}\right) \qquad [3]$$

tends toward zero at low frequencies, indicating that the current and potential are in phase. The phase angle tends toward zero at high frequencies as well, due to the influence of the leading resistor R_e in the value of Z_r used in Eq. 3. Dashed lines in Fig. 2b and c indicate the characteristic frequencies associated with the time constants of the synthetic impedance data of Table I. No clear correspondence is seen between the Bode plots and the time constants of the impedance data.

The popularity of the Bode representation stems from its utility in circuits analysis. The phase-angle plots are sensitive to system parameters and, therefore, provide a good means of comparing the model to experiment. The modulus is much less sensitive to system parameters, but the asymptotic values at low and high frequencies provide values for the dc and electrolyte resistance, respectively.

Table I. Randles circuit parameters.

R_e (Ω cm^2)	R_t (Ω cm^2)	Q_{dl} (MΩ^{-1} cm^{-2} s$^\alpha$)	α	τ_d/s	$z_d(0)$ (Ω cm^2)
100	100	15.915	1.0	1	1000
100	100	109.97	0.7	1	1000
100	100	398.94	0.5	1	1000

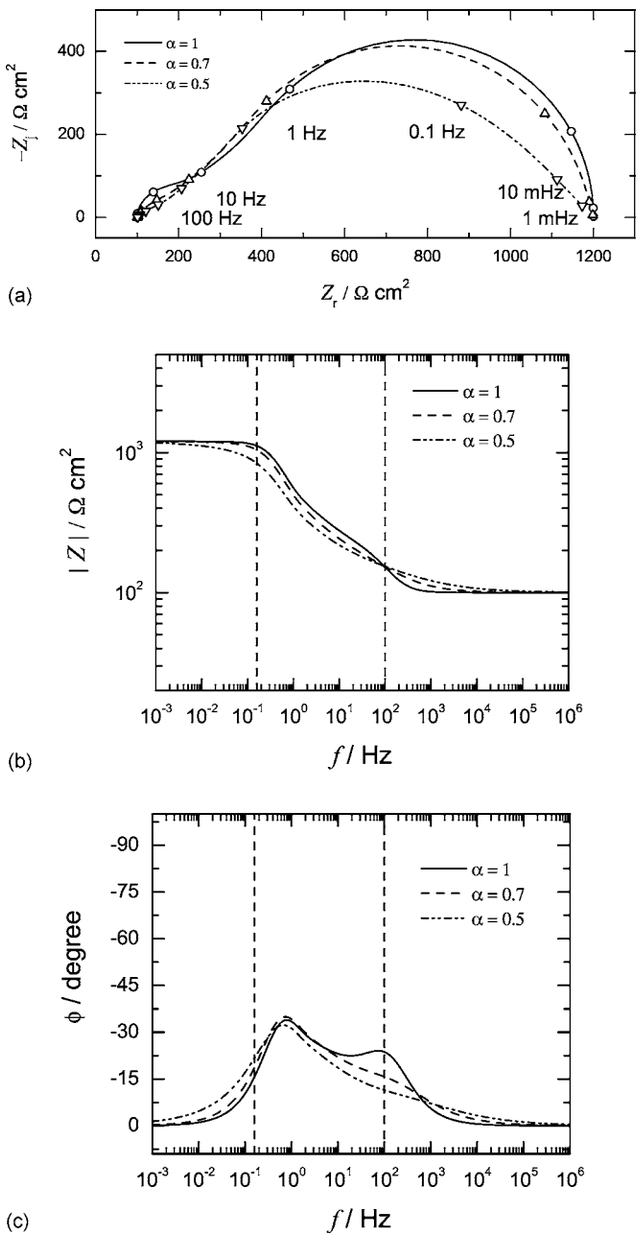

Figure 2. Traditional representation of impedance data for the Randles circuit presented as Fig. 1a with α as a parameter. (a) Complex-impedance-plane or Nyquist representation (symbols are used to designate decades of frequency; (b) Bode representation of the magnitude of the impedance; and (c) Bode representation of the phase angle.

For electrochemical systems exhibiting an ohmic or electrolyte resistance, however, the Bode representation has serious drawbacks. The influence of electrolyte resistance confounds the use of phase-angle plots, such as shown in Fig. 2c, to estimate characteristic frequencies. In addition, Fig. 2c shows that the current and overpotential are in-phase at high frequencies; whereas, at high frequencies, for $\alpha = 1$, the current and surface potential are exactly out of phase. Even when $\alpha \neq 1$, the current and surface potential are not in-phase at high frequencies. The electrolyte resistance, then, obscures the behavior of the electrode surface in the phase-angle plots.

Phase angle and modulus corrected for ohmic resistance.— If an accurate estimate for electrolyte resistance $R_{e,est}$ is available, a modified Bode representation is possible following

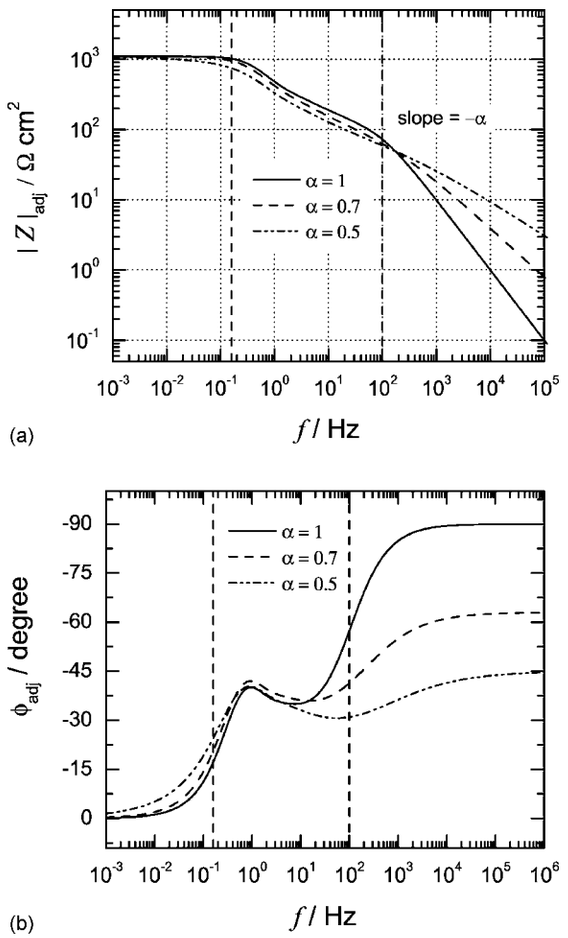

Figure 3. Bode plots with α as a parameter for the Randles circuit presented as Fig. 1a adjusted for the electrolyte resistance following Eq. 4 and 5: (a) modulus; (b) phase angle.

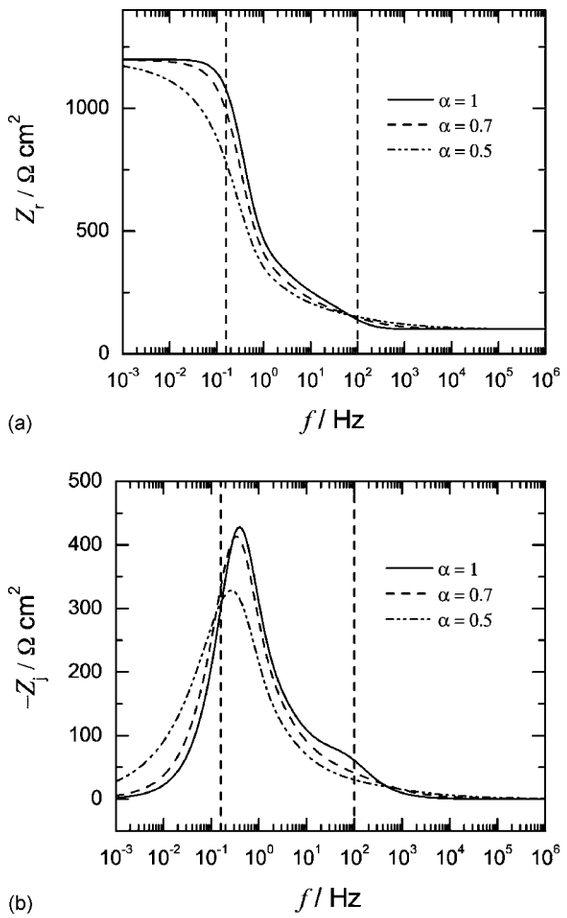

Figure 4. Real and imaginary parts of the impedance as a function of frequency with α as a parameter for the Randles circuit presented as Fig. 1a: (a) real part; (b) imaginary part.

$$\phi_{adj} = \tan^{-1}\left(\frac{Z_j}{Z_r - R_{e,est}}\right) \quad [4]$$

and

$$|Z|_{adj} = \sqrt{(Z_r - R_{e,est})^2 + (Z_j)^2} \quad [5]$$

The results are presented in Fig. 3a and b for magnitude and phase angle, respectively.

The slope of the corrected modulus yields valuable information concerning the existence of CPE behavior that is obscured in the traditional Bode presentation. At high frequencies, the corrected modulus is dominated by the contribution of the imaginary part of the impedance. The corrected modulus approaches zero according to $|Z|_{adj} \sim f^{-\alpha}$; thus, the slope on a logarithmic plot has a value of $-\alpha$ at high frequencies.

As seen in Fig. 3b, for systems exhibiting purely capacitive behavior, i.e., where $\alpha = 1$, the current and potential are in-phase at low frequencies and out-of-phase at high frequencies. The phase angle has an inflection point at the characteristic frequency f_{RC} = 100 Hz and reaches a value of −90° at high frequency. Under conditions in which CPE behavior is evident, i.e., when $\alpha \neq 1$, the phase angle reaches a high-frequency asymptote such that

$$\phi_{adj}(\infty) = -90\alpha \quad [6]$$

The corrected phase-angle plots yield valuable information concerning the existence of CPE behavior that is obscured in the traditional Bode presentation.

Caution should be used when interpreting electrolyte-resistance-corrected Bode plots. Incorrect estimates for $R_{e,est}$ can give the appearance of an additional high-frequency relaxation process. When possible, an assessment of $R_{e,est}$ should be made independently of the regression. In addition, noise in the experimental data can obscure the behavior of the corrected phase angle at high frequencies. At high frequencies, $Z_r \rightarrow R_{e,est}$. Thus, the argument to the inverse tangent in Eq. 4 will have a sign controlled by noise in the denominator, and the phase calculated from Eq. 4 will have values scattered about $\pm\phi_{adj}(\infty)$. This scatter will of course be evident as well in the ohmic-resistance-corrected magnitude plots. Nevertheless, Bode plots corrected for ohmic resistance are useful as a pedagogical tool and for determining whether CPE behavior is evident in the data.

Real and imaginary components.— The difficulty with using the ohmic-resistance-corrected Bode plots presented in the previous section is that an accurate estimate is needed for the electrolyte resistance and that, at high frequencies, the difference $Z_r - R_{e,est}$ is determined by stochastic noise. These difficulties can be obviated by plotting the real and imaginary components of the impedance (see, for example, Betova et al.[17]). The real part of the impedance, shown in Fig. 4a, provides the same information as is available from the modulus plots presented in Fig. 2b. The high-frequency asymptote reveals the ohmic electrolyte resistance, and the low-frequency asymptote reveals the sum of the polarization impedance and the electrolyte resistance. The imaginary part of the impedance, presented in Fig. 4b, has the significant advantage that the characteristic

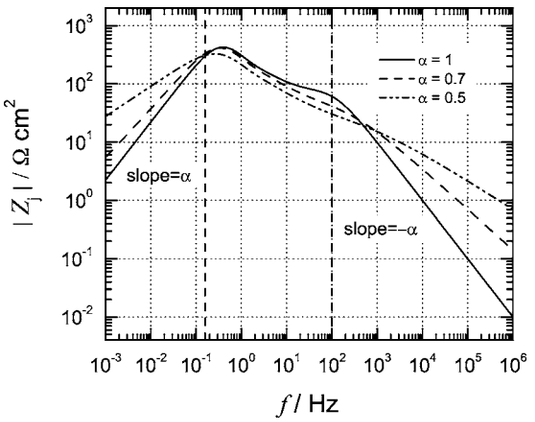

Figure 5. Imaginary part of the impedance as a function of frequency with α as a parameter for the Randles circuit presented as Fig. 1a.

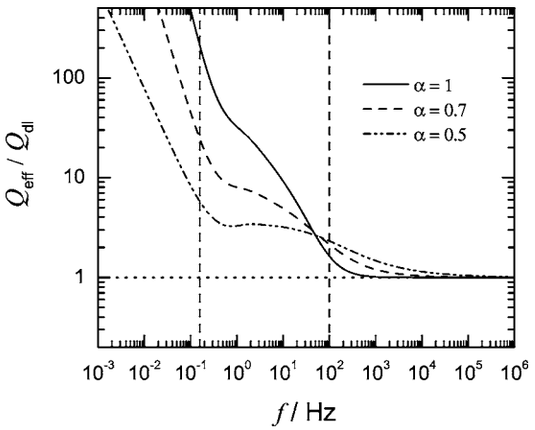

Figure 6. Effective CPE coefficient defined by Eq. 7, scaled by the input value of the double-layer CPE coefficient, as a function of frequency with α as a parameter for the Randles circuit presented as Fig. 1a.

frequencies can be readily identified at the peak values. The imaginary part of the impedance is independent of electrolyte resistance, so correction for ohmic resistance is not needed.

The behavior at lower impedance values is emphasized when the impedance components are plotted on a logarithmic scale, as shown in Fig. 5. Figure 5 provides a rich source of insight into the experimental system. As in Fig. 4b, a characteristic frequency can be defined to exist at the maximum value. The slopes at low and high frequency are $+\alpha$ and $-\alpha$, respectively. Departure from ± 1 provides an indication of distributed processes. Observation of multiple maxima shows that the data must be interpreted in terms of more than one process. Interpretation of Fig. 5 in terms of characteristic frequencies is not confounded by the electrolyte resistance, as was seen for the Bode plots of phase angle.

As discussed elsewhere,[18-21] the variances of stochastic errors are equal for real and imaginary parts of the impedance. Thus, another advantage of presenting real and imaginary parts of the impedance as functions of frequency is that comparison between data and levels of stochastic noise can be easily represented.

Effective high-frequency capacity or CPE coefficient.— An effective capacitance, or when $\alpha \neq 1$, an effective CPE coefficient may be obtained directly from the imaginary part of the impedance as

$$Q_{\text{eff}} = \sin\left(\frac{\alpha\pi}{2}\right)\frac{-1}{Z_j(f)(2\pi f)^{\alpha}} \qquad [7]$$

When $\alpha = 1$, the CPE coefficient Q becomes a capacitance, and Eq. 7 can be written

$$Q_{\text{eff}} = C_{\text{eff}} = \frac{-1}{Z_j(f)(2\pi f)} \qquad [8]$$

The ratio of effective CPE coefficient to the expected value is given in Fig. 6. The high-frequency asymptote is seen to provide correct values for the double-layer CPE coefficient, Q_{dl}. The assessment should be made at frequencies significantly larger than the largest characteristic relaxation frequency for the system. At frequencies only one order of magnitude larger than f_{RC}, the error in assessment of the double-layer CPE coefficient is only 1% for $\alpha = 1$. Measurement at several different frequencies should be used to ensure that the CPE coefficient is obtained at a frequency sufficiently larger than the largest characteristic relaxation frequency for the system.

Application to blocking electrodes.— The impedance of the blocking circuit presented in Fig. 1b is given by

$$Z(f) = R_e + \frac{1}{(j2\pi f)^{\alpha}Q} \qquad [9]$$

The parameter values R_e, α, and Q used for the simulations presented here are the same as those given for the Randles circuit in Table I.

Nyquist and Bode representations.— The complex impedance plane or Nyquist representation of the impedance for the blocking electrode of Fig. 1b is presented in Fig. 7a. For $\alpha = 1$, the real part of the impedance for the blocking circuit is equal to R_e for all frequencies. The tendency of the imaginary part to approach $-\infty$ as frequency tends toward zero appears as a vertical line in the impedance plane plot given as Fig. 7a. For $\alpha \neq 1$, the real and imaginary parts tend toward $+\infty$ and $-\infty$, respectively, showing that, in contrast to the impedance of reactive systems, a finite dc limit is not seen. Under dc conditions, current cannot pass. The high-frequency limit, not visible on the scale presented, has a value of R_e for all values of α.

The Bode representation is presented in Fig. 7b and c for modulus and phase angle, respectively. The traditional values of modulus and phase angle are compared to the values adjusted for the electrolyte resistance following Eq. 4 and 5.

The magnitude, presented in Fig. 7b, tends toward R_e as frequency tends toward ∞ and toward ∞ as frequency tends toward zero. The slope of the line at low frequencies has a value of $-\alpha$ for the blocking electrode. Slopes with values smaller than unity could provide an indication of a blocking electrode with a distribution of characteristic time constants. The slope of the modulus corrected for ohmic resistance is equal to $-\alpha$ for all frequencies.

The phase angle for the blocking configuration, shown in Fig. 7c, tends toward a constant value of -90α degrees at low frequencies and toward zero at high frequencies. As seen for the reactive system in Fig. 2c, the behavior at high frequencies is attributed to the confounding influence of the electrolyte resistance. The corrected phase angle is constant for all frequencies, with a value of -90α degrees as is shown in Fig. 7c. Again, accurate estimates for the ohmic resistance are needed to generate the corrected plots.

Imaginary component.— The logarithm of the imaginary part of the impedance is presented in Fig. 8. The imaginary part of the impedance presented in Fig. 8 is identical to the ohmic-resistance-corrected modulus presented in Fig. 7b, but has the advantage that it can be obtained directly without need for an estimate of the electrolyte resistance. The slope of the imaginary part of the impedance on a logarithmic plot is independent of frequency and has a value of $-\alpha$.

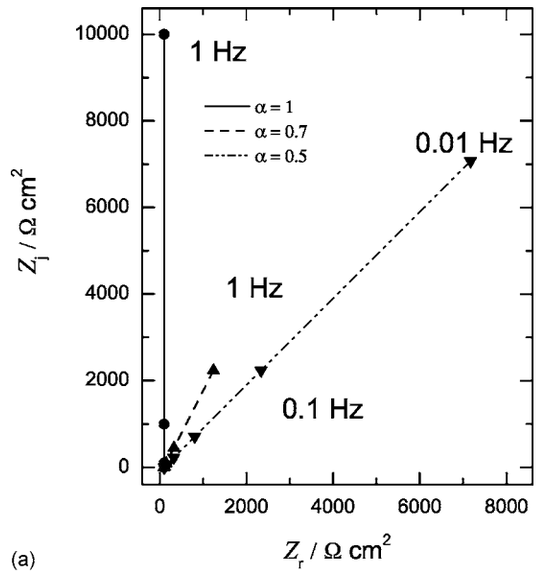

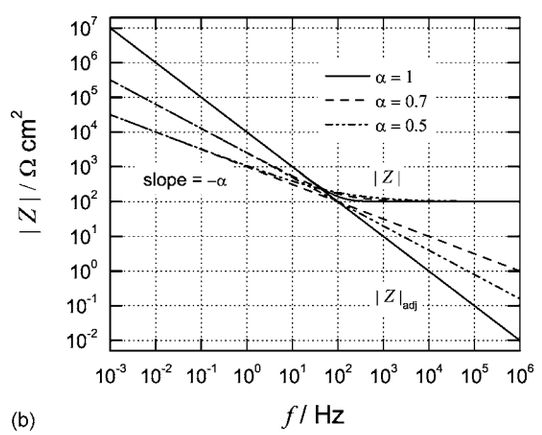

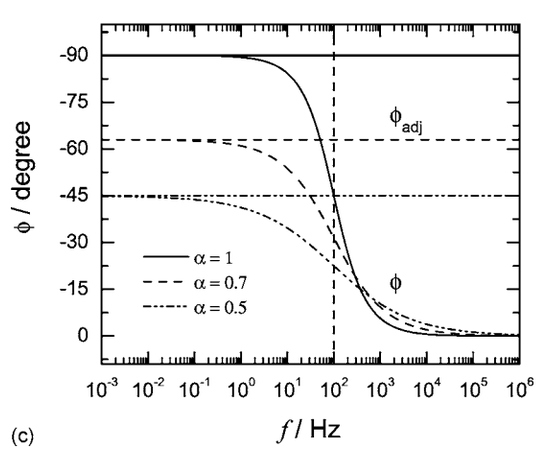

Figure 7. Nyquist and Bode representations of impedance data for the blocking circuit presented as Fig. 1b with α as a parameter. (a) Complex-impedance-plane or Nyquist representation (symbols are used to designate decades of frequency; (b) Bode representation of the magnitude of the impedance; and (c) Bode representation of the phase angle.

Effective CPE coefficient.— The ratio of effective CPE coefficient, calculated using Eq. 7, to the expected value is given in Fig. 9. The effective CPE coefficient is seen to be independent of frequency.

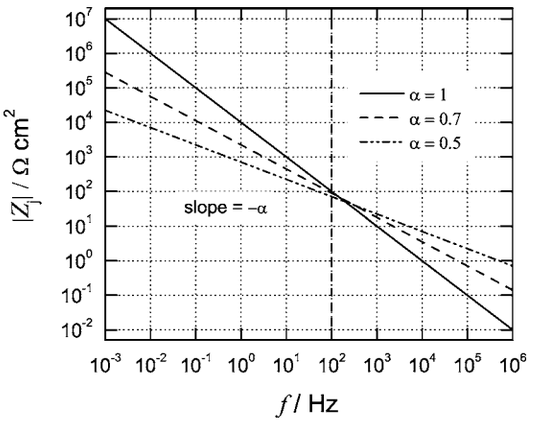

Figure 8. Imaginary part of the impedance as a function of frequency with α as a parameter for the blocking circuit presented as Fig. 1b.

Application to Experimental Data

In a recent study, the corrosion behavior of as-cast magnesium alloys (AM50 and AZ91) was investigated in a sodium sulfate solution by electrochemical impedance spectroscopy.[22] At the corrosion potential and for short immersion times (<6 h), the impedance diagrams presented the same features as that obtained for pure magnesium.[23,24] Thus, in spite of the presence of coarse metallic particles (Mg-Al, Mg-Al-Zn, and Mg-Al-Mn) in the matrix of the alloys and of eutectic areas in grain boundaries of the AZ91 alloy, the corrosion behavior of the alloys was similar to that of pure magnesium. This was explained by the fact that, at the beginning of immersion, the coarse intermetallic particles and the eutectic areas remained unaffected due to galvanic coupling between these zones and the grain body. Thus, for short immersion times, the impedance diagrams represent the corrosion process in the grain body because both the coarse particles and the eutectic areas are cathodic, protecting them against corrosion.

The anodic dissolution of magnesium is characterized by an unusual phenomenon called a "negative difference effect" (NDE). It is found experimentally that, when the anodic overvoltage is increased, the cathodic hydrogen evolution reaction unexpectedly increases. To explain the magnesium corrosion and more particularly the NDE phenomenon, several mechanisms have been proposed including the formation of magnesium hydride, metastable monovalent ions, or magnesium hydroxide or oxide. Song et al.[25-27] proposed recently a

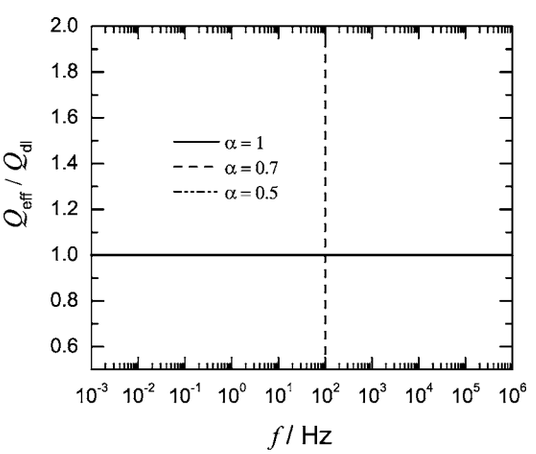

Figure 9. Effective CPE coefficient defined by Eq. 7, scaled by the input value of the double-layer CPE coefficient, as a function of frequency with α as a parameter for the blocking circuit presented as Fig. 1b.

new mechanism for the NDE. They explained that the formation of a partially protective layer of $Mg(OH)_2$ plays an important role in the corrosion behavior of magnesium. Their mechanism is based on an increase in the film-free areas with increasing anodic potential on which the anodic and cathodic partial reactions can occur more easily than on the surface covered by a film. They assumed that magnesium corrosion occurs on film-free areas with the production of univalent ions. For high anodic overpotentials, the rate of the chemical reaction is increased due to the increased concentration of Mg^+ due to dissolution of Mg, and, concomitantly, there is an increase in the amount of hydrogen evolved. Song et al.[25-27] mentioned that the protective film is potential-dependent in that there is complete film coverage over the whole surface and a low rate of corrosion for potentials below the pitting potential.

Experimental approach.— In the present work, the graphical methods described in the previous section are used to establish a preliminary description of the data. The experimental design and preliminary data analysis are presented in this section.

Material.— The magnesium alloy AZ91 was studied in the form of as-cast ingots supplied by Pechiney. Etching treatments revealed a heterogeneous microstructure increasing from the center to the edge of the ingots and, as a consequence, the samples were taken from the central zone of the ingots, resulting in more homogenous, equiaxed grain samples. The AZ91 working electrode consisted of a rotating disk with an exposed area of 1 cm^2. The shaft was covered with a heat-shrinkable sheath. Before the experiments, the surface was polished with SiC paper (grade 4000), cleaned in distilled water in an ultrasonic bath, and dried in warm air. The corrosive medium was a 0.1 M solution of NaCl (reagent grade) in contact with air, maintained at 25°C.

Electrochemical measurements.— The auxiliary electrode was a platinum grid with a large surface area, and the reference was a saturated calomel electrode (SCE). Electrochemical impedance measurements were carried out using a Solartron 1286 electrochemical interface and a Solartron 1250 frequency response analyzer. The measured frequency range was 65 kHz to a few mHz. The impedance diagrams were obtained at a rotation rate of 240 rpm after different immersion times at the corrosion potential.

Measurement model analysis.— The measurement model analysis developed by Agarwal et al.[19,28,29] was applied to the impedance data. The standard deviation of the stochastic errors ranged from 0.2% of the modulus at high frequency to 0.75% at the lowest frequency measured. An error-structure-weighted regression of the measurement model to the imaginary component of the impedance was used to assess consistency with the Kramers-Kronig relations. All data were found to be consistent with the Kramers-Kronig relations. A feature found at high frequencies was attributed to instrumental artifacts; thus, the experimental frequency ranged used for this study was truncated to 0.076 Hz to 15.5 kHz.

Traditional representation of data.— Impedance data are often represented in complex-impedance-plane or Nyquist formats accompanied with Bode representations in which the modulus and phase angle are presented as a function of frequency. Such traditional representations of impedance data are given in Fig. 10 for the AZ91 alloy at the corrosion potential after different immersion times in 0.1 M NaCl.

Physical model.— According to the previous studies,[22-24] the high-frequency loop appears to result from both charge transfer and a film effect of corrosion products because the value of the capacitance associated with this loop is low (around 10 $\mu F\ cm^{-2}$) and below the usual value of a double-layer capacitance (around 50 $\mu F\ cm^{-2}$). The medium frequency capacitive loop was attributed to relaxation of mass transport in the solid phase due to the growth of the corrosion product layer $[MgO/Mg(OH)_2]$. The inductive loop may be due to the occurrence of relaxation processes of adsorbed species such as Mg^+_{ads}. The modification of the impedance diagrams

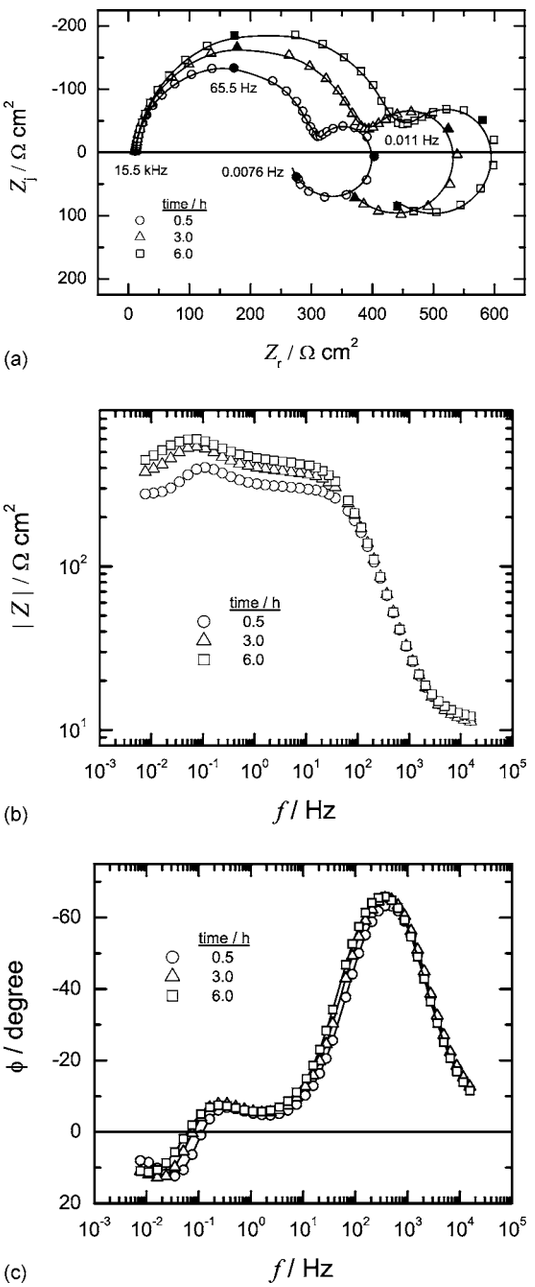

Figure 10. Traditional representation of impedance data obtained for the AZ91 alloy at the corrosion potential after different immersion times in 0.1 M NaCl: (a) complex-impedance-plane or Nyquist representation (the lines represent the measurement model fit to the complex data sets; (b) Bode representation of the magnitude of the impedance as a function of frequency; and (c) Bode representation of the phase angle as a function of frequency.

with time of sample immersion is likely due to an improvement of the protection of the surface by the corrosion products.

Alternative graphical representation of data.— The imaginary part of the impedance is plotted on a logarithmic scale in Fig. 11. A line with slope -0.856 ± 0.007 is shown, which was fitted to the high-frequency data for $t = 0.5$ h of immersion. This slope has the value of $-\alpha$, and departure from -1 provides an indication of distributed processes. The low-frequency portion of the high-frequency capacitive loop has a slope of 0.661 ± 0.008. The lack of symmetry suggests that the high-frequency capacitance is in parallel with other

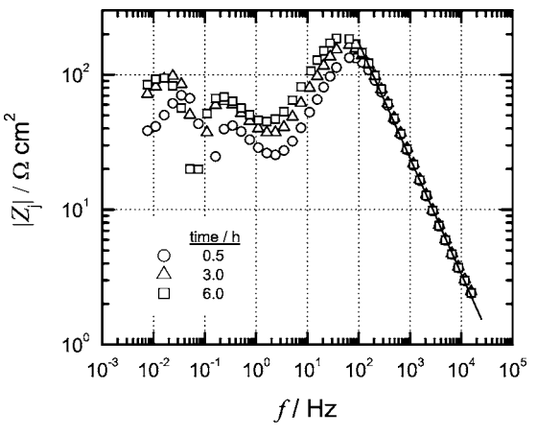

Figure 11. Imaginary part of the impedance as a function of frequency for the AZ91 alloy at the corrosion potential after different immersion times in 0.1 M NaCl. The line with slope −0.856 ± 0.007 was fitted to the high-frequency data for t = 0.5 h of immersion time.

reactive processes. Observation of multiple maxima also shows that the data must be interpreted in terms of more than one process.

The slopes at the high-frequency asymptotes appear to be in good agreement for the three data sets, but a more detailed analysis reveals some trending. Values for the CPE exponent are provided in Table II. A small increase in the value of α is evident as the immersion time increases.

The value of α can be used in Eq. 7 to obtain an apparent CPE coefficient Q_{eff}. The resulting values of Q_{eff} are presented in Fig. 12. The absence of a clearly identifiable asymptote may be attributed to high-frequency instrumental artifacts. The values for the CPE coefficient provided in Table II represent the average over the values for the 10 highest frequencies. A small reduction in the value of Q_{eff} is evident as the immersion time increases.

The value of α obtained from Fig. 11 can also be used to find the solution resistance R_e used in Eq. 4 to yield the expected asymptotic value for the adjusted phase angle given by Eq. 4. The resulting ohmic-resistance-corrected phase angle and magnitude are given in Fig. 13. The slope of the high-frequency asymptote for magnitude corrected for electrolyte resistance has a value of −α. Values for the electrolyte resistance are provided in Table II.

Discussion

The graphical representations presented here are intended to enhance analysis and to provide guidance for the development of appropriate physical models. While visual inspection of data alone cannot provide all the nuance and detail that can, in principle, be extracted from impedance data, the graphical methods described in the present work can provide both qualitative and quantitative evaluation of electrochemical impedance data.

The impedance plane or Nyquist plots presented as Fig. 2a, 7a, and 10a provide a sense of the type of processes which govern the low-frequency behavior of the system. The shape of the low-frequency loop in Fig. 2a is typically associated with mass transfer effects, although the shape is clearly distorted by the CPE behavior for $\alpha < 1$. A blocking behavior is suggested by the absence of a low-frequency (dc) limit in Fig. 7a. Three time constants are clearly evident in Fig. 10a.

Aside from values for asymptotic limits for the real part of the impedance, it is difficult to extract meaningful information from the traditional Bode plots when the Ohmic resistance is not negligible.

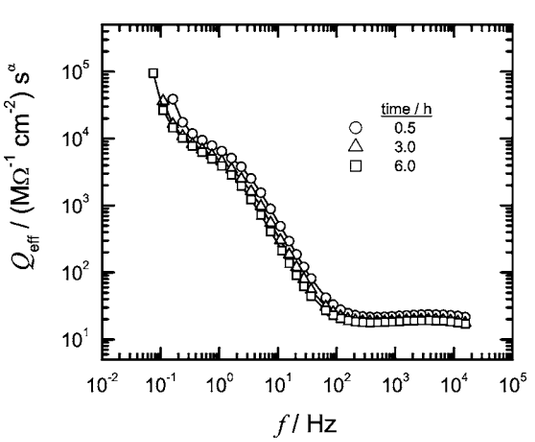

Figure 12. Effective CPE coefficient defined by Eq. 7 for the AZ91 alloy at the corrosion potential after different immersion times in 0.1 M NaCl.

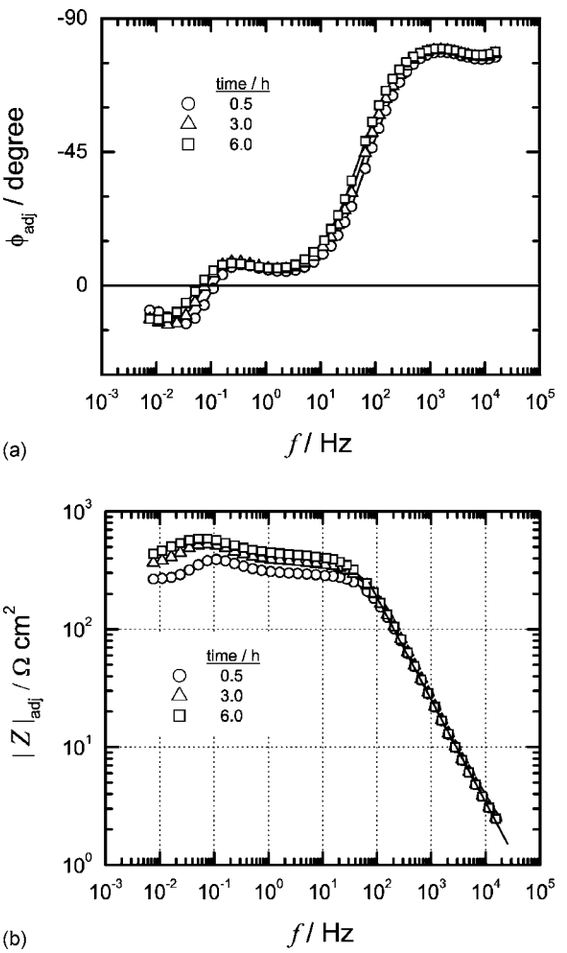

Figure 13. Ohmic-resistance-corrected Bode plots for the AZ91 alloy at the corrosion potential after different immersion times in 0.1 M NaCl, with values adjusted for the electrolyte resistance following Eq. 4: (a) phase angle; (b) modulus.

Table II. Values for the high-frequency component obtained from asymptotic values.

Immersion time (h)	0.5	3.0	6.0
α (dimensionless)	0.856	0.872	0.877
Q_{eff} (MΩ^{-1} cm^{-2} s$^{\alpha}$)	22.7	19.1	18.5
R_e (Ω cm^2)	10.65	10.45	11.4

In contrast, the Bode plots of magnitude and phase angle corrected for Ohmic resistance can be used to identify CPE behavior at high frequencies. Following Eq. 6, the high-frequency limit for the phase angle (Fig. 3b and 13a) can be used to extract values for the CPE coefficient α. The Ohmic-resistance-corrected phase angle for the blocking system shown in Fig. 7c is constant for all frequencies. The slope of the corrected modulus (Fig. 3a, 7b, and 13b) can also be used to extract values for the CPE coefficient α.

The plots of the imaginary part of the impedance on a logarithmic scale shown in Fig. 5 and 11 are particularly helpful. The slopes of the lines at low and high frequency in Fig. 5 indicate clearly that two time constants can be discerned, that the high-frequency feature has CPE characteristics, and that the CPE characteristic extends to the low-frequency feature. This result indicates that the two time constants are coupled through a double-layer capacitive or constant-phase element. Log-log plots of imaginary impedance can be used to distinguish between a depressed impedance plane semicircle caused by a continuous distribution of time constants associated with a CPE and that caused by contributions of discrete processes with closely overlapping but discrete time constants.

For the AZ91 data, the logarithm of the imaginary part of the impedance shown in Fig. 11 indicated a CPE behavior, meaning that the high-frequency feature had the characteristic of a distributed time constant rather than several discrete time constants. The absence of symmetry for the high-frequency feature suggested that the capacitive behavior was in parallel to other reactive processes. The decrease in α with immersion time suggests that the surface became more homogeneous with the growth of corrosion product layers.

For the blocking system, the plot of the imaginary part of the impedance on a logarithmic scale shown in Fig. 8 yields the same information as the Ohmic-resistance-corrected modulus presented in Fig. 7b. The advantage of using Fig. 8 is that no estimate is needed for the electrolyte resistance.

The effective CPE coefficient representation in Fig. 6 and 12 yields, for $\alpha = 1$, information concerning the high-frequency capacitance of the system. In the case that $\alpha < 1$, Fig. 6 and 12 yield an effective CPE coefficient Q_{eff} which can be related to the film capacitance through a model of the distributed time constants following Brug et al.[8]

The plots presented here have general application. They have been useful for evaluating the high-frequency behavior associated with local impedance measurements, where low-frequency measurements were not reliable and the frequency range was therefore not sufficient to allow regression analysis with a detailed mathematical model.[30] The graphical analysis showed that, while high-frequency CPE behavior was evident in global impedance measurements for a Mg AZ91 alloy disk electrode, the local impedance measured near the center of the disk exhibited ideal *RC* behavior. The CPE behavior was thereby attributed to a 2D radial distribution of the charge-transfer resistance. The capacitance extracted from high-frequency asymptotic behavior was used to estimate the area sampled by the local impedance technique.

The graphical methods presented in this paper for visualizing and interpreting electrochemical impedance data can be applied by using the same concepts to other quantities such as admittance,[31] complex capacitance,[32] and generalized transfer functions[33] such as electrohydrodynamic impedance.[3]

Conclusions

Ohmic-resistance-corrected Bode plots, logarithmic plots of the imaginary component of the impedance, and effective capacitance plots are useful complements to the more traditionally used complex-impedance-plane and Bode representations for impedance data. Bode plots, in particular, are confounded by the influence of electrolyte resistance. The plots proposed here provide useful guides to model development for both reactive and blocking systems.

Acknowledgment

The authors gratefully acknowledge Jean-Baptiste Jorcin, who performed the measurements on the AZ91 alloy.

The University of Florida assisted in meeting the publication costs of this article.

References

1. M. H. Dean and U. Stimming, *J. Electroanal. Chem. Interfacial Electrochem.*, **228**, 135 (1987).
2. B. Tribollet, J. Newman, and W. H. Smyrl, *J. Electrochem. Soc.*, **135**, 134 (1988).
3. C. Deslouis and B. Tribollet, in *Advances in Electrochemical Science and Engineering*, H. Gerischer and C. W. Tobias, Editors, p. 205, VCH, New York (1991).
4. A. N. Jansen, P. T. Wojcik, P. Agarwal, and M. E. Orazem, *J. Electrochem. Soc.*, **143**, 4066 (1996).
5. D. D. Macdonald, *Transient Techniques in Electrochemistry*, Plenum Press, New York (1977).
6. C. Gabrielli, *Solartran Instrumentation Group Monograph*, The Solartran Electronic Group Ltd., Farnborough, England (1980).
7. J. R. Macdonald, *Impedance Spectroscopy: Emphasizing Solid Materials and Systems*, John Wiley & Sons, New York (1987).
8. G. J. Brug, A. L. G. V. den Eeden, M. Sluyters-Rehbach, and J. H. Sluyters, *J. Electroanal. Chem. Interfacial Electrochem.*, **176**, 275 (1984).
9. A. Lasia, in *Modern Aspects of Electrochemistry*, R. E. White, B. E. Conway, and J. O. Bockris, Editors, Vol. 32, p. 143, Plenum Press, New York (1999).
10. Z. Lukacs, *J. Electroanal. Chem.*, **432**, 79 (1997).
11. Z. Lukacs, *J. Electroanal. Chem.*, **464**, 68 (1999).
12. J. R. Macdonald, *J. Appl. Phys.*, **58**, 1971 (1985).
13. J. R. Macdonald, *J. Appl. Phys.*, **58**, 1955 (1985).
14. R. L. Hurt and J. R. Macdonald, *Solid State Ionics*, **20**, 111 (1986).
15. J. R. Macdonald, *J. Appl. Phys.*, **62**, R51 (1987).
16. J. R. Macdonald, *J. Electroanal. Chem.*, **378**, 17 (1994).
17. I. Betova, M. Bojinov, T. Laitinen, K. Malela, P. Pohjanne, and T. Saario, *Corros. Sci.*, **44**, 2699 (2002).
18. M. Orazem, P. Agarwal, A. N. Jansen, P. T. Wojcik, and L. H. García-Rubio, *Electrochim. Acta*, **38**, 1903 (1993).
19. P. Agarwal, O. D. Crisalle, M. E. Orazem, and L. H. García-Rubio, *J. Electrochem. Soc.*, **142**, 4149 (1995).
20. M. E. Orazem, T. E. Moustafid, C. Deslouis, and B. Tribollet, *J. Electrochem. Soc.*, **143**, 3880 (1996).
21. S. L. Carson, M. E. Orazem, O. D. Crisalle, and L. H. García-Rubio, *J. Electrochem. Soc.*, **150**, E477 (2003).
22. G. Baril, C. Blanc, and N. Pébère, *J. Electrochem. Soc.*, **148**, B489 (2001).
23. N. Pébère, C. Riera, and F. Dabosi, *Electrochim. Acta*, **35**, 555 (1990).
24. G. Baril and N. Pébère, *Corros. Sci.*, **43**, 471 (2001).
25. G. Song, A. Atrens, D. St. John, J. Nairn, and Y. Li, *Corros. Sci.*, **39**, 855 (1997).
26. G. Song, A. Atrens, D. St. John, X. Wu, and J. Nairn, *Corros. Sci.*, **39**, 1981 (1997).
27. G. Song and A. Atrens, *Adv. Eng. Mater.*, **5**, 837 (2003).
28. P. Agarwal, M. E. Orazem, and L. H. García-Rubio, *J. Electrochem. Soc.*, **139**, 1917 (1992).
29. P. Agarwal, M. E. Orazem, and L. H. García-Rubio, *J. Electrochem. Soc.*, **142**, 4159 (1995).
30. J.-B. Jorcin, M. E. Orazem, N. Pébère, and B. Tribollet, *Electrochim. Acta*, **51**, 1473 (2006).
31. J. R. Macdonald and J. A. Garber, *J. Electrochem. Soc.*, **124**, 1022 (1977).
32. P. L. Taberna, P. Simon, and J. F. Fauvarque, *J. Electrochem. Soc.*, **150**, A292 (2003).
33. C. Gabrielli and B. Tribollet, *J. Electrochem. Soc.*, **141**, 1147 (1994).